Available online at www.sciencedirect.com
ScienceDirect
Medical Image Analysis 12 (2008) 217–227
MEDICAL IMAGE ANALYSIS
www.elsevier.com/locate/media

Spherical harmonics-based parametric deconvolution of 3D surface images using bending energy minimization

Khaled Khairy *, Jonathon Howard

Max Planck Institute of Molecular Cell Biology and Genetics, 01307 Dresden, Germany

Received 25 July 2006; received in revised form 27 September 2007; accepted 12 October 2007
Available online 30 October 2007

Abstract

Numerical deconvolution of 3D fluorescence microscopy data yields sharper images by reversing the known optical aberrations introduced during the acquisition process. When additional prior information such as the topology and smoothness of the imaged object surface is available, the deconvolution can be performed by fitting a parametric surface directly to the image data. In this work, we incorporate such additional information into the deconvolution process and focus on a parametric shape description suitable for the study of organelles, cells and tissues. Such membrane-bound closed biological surfaces are often topologically equivalent to the sphere and can be parameterized as series expansions in spherical harmonic functions (SH). Because image data are noisy and the SH-parameterization is prone to the formation of high curvatures even at low expansion orders, the parametric deconvolution problem is ill-posed and must be regularized. We use the shape bending energy as a regularizing (smoothing) function, and determine the regularization parameter graphically with the help of the L-curve method. We demonstrate the complete deconvolution scheme, including the initial image segmentation, the calculation of a good starting surface and the construction of the L-curve, using real and synthetic image data.

Keywords: Spherical harmonics; Shape parameterization; Fluorescence microscopy; Image segmentation; Image reconstruction; Deconvolution; Shape modelling; L-curve; Inverse problems; Parametric deconvolution; Cell morphology

1. Introduction

Image deconvolution is a computational process in which the measured or estimated point spread function (PSF) of an optical instrument such as a microscope is used to partially reverse optical distortions (Jansson, 1996; Verveer et al., 1999). It is especially beneficial in three dimensions (3D) where out-of-focus light can lead to pronounced image degradation. Deconvolution takes advantage of prior information about the physics of image formation in the microscope. However, there is often additional prior information contained within the images themselves and that is not generally used in image deconvolution.

Common examples in cell biology of 3D images with prior information are those of cells and organelles. Cells and organelles have diverse, often complex shapes for which there is no "golden standard"; this makes the accurate measurement of their morphology experimentally and theoretically challenging. However, we know that (a) the surfaces of cells and organelles are topologically closed, because of the exceedingly high energy associated with unsealed membranes, (b) cells and organelles are often topologically equivalent to the surface of the sphere (they are therefore binary objects in the sense that each point is either inside, outside or at the boundary), and (c) the bending stiffness of the bounding membrane together with its associated cytoskeleton smoothen the surface. This prior information is not used in conventional image deconvolution, which

Abbreviations: SH, spherical harmonics; SHP, spherical harmonics parameterization; RBC, red blood cell; PSF, point spread function; RBF, radial basis function.

* Corresponding author. Present address: European Molecular Biology Lab (EMBL) Heidelberg, Meyerhofstrasse 1, D-69117 Heidelberg, Germany. Tel.: +49 6221 387 8123.
E-mail address: khairy@embl.de (K. Khairy).

1361-8415/$ - see front matter © 2007 Elsevier B.V. All rights reserved.
doi:10.1016/j.media.2007.10.005

simply produces a sharper image that must subsequently be segmented to obtain the surface of interest.

The prior information about the topology of a 3D object can be utilized by parameterizing the shape mathematically (Terzopoulos et al., 1988; Staib and Duncan, 1996). The question then becomes: which surface best fits the measured image? If a smoothness assumption can be made to make this inverse problem well posed, then the optimal set of shape surface parameters would be a solution to the deconvolution problem that solves both the image-sharpening and surface-finding problems simultaneously. We call this type of deconvolution "parametric deconvolution", as opposed to the usual numerical "non-parametric deconvolution". Parametric deconvolution does not produce a sharper image in the conventional sense, but directly outputs the most probable underlying mathematical surface.

In this work, we focus on the common case when the shapes under study are topologically equivalent to the sphere. A subset of such surfaces can be parameterized by spherical curves in which the radial distance is a function of the longitude and latitude. Such curves can be represented by a spherical harmonics (SH) series, a three-dimensional generalization of the Fourier series for line curves, and affords a natural way to smooth the surfaces by truncation of the series. However spherical curves only describe "stellar" shapes for which there is an internal point that "sees" all the points on the surface without crossing the surface. This limits the applicability of spherical curves because many cells and organelles of interest are not stellar. To circumvent this limitation, we use the spherical harmonics parameterization (SHP), developed by Brechbühler et al. (1995) for 3D image analysis. The SHP represents the surface as spherical harmonics series expansions of the individual x, y and z Cartesian coordinates of the surface and parameterizes both stellar and non-stellar surfaces. It has been applied in various contexts by Gerig, Styner and colleagues (Sezekely et al., 1996; Kelemen et al., 1999; Gerig et al., 2001; Styner et al., 2005). The SHP has two additional advantages: it can generate a wide variety of shapes with a small number of parameters, and it offers straightforward calculations of the geometrical properties of a surface such as area, enclosed volume and curvature. These geometrical properties are important descriptors of cell morphology. For example, changes in volume and area are often used to characterize the effects of perturbations or mutations on cells (e.g. hereditary blood diseases); and the curvature of the membrane is important because it can determine which lipids or proteins will partition into it (McMahon and Gallop, 2005) and the mean-squared curvature is proportional to the energy required to deform the cell (Lipowsky, 1991). Both the area and curvature are difficult to measure because they depend on the contour derivatives. The SHP does suffer from a disadvantage: it allows for surfaces with regions of high curvature even at low SH-expansion orders and therefore requires a strong smoothing constraint to yield realistic surfaces.

In this paper, we describe a method to analyze 3D microscopy surface images quantitatively using SH-based parametric deconvolution. The surface is detected either by using a fluorescent dye that labels the membrane or a cytoplasmic dye that labels the inside of the cell, although in this study we only give examples of membrane-labelled objects. In order to make the surface-determination problem well defined and exclude surfaces with unrealistic high curvatures, we used the L-curve method (Hansen, 1997) to choose the balance between smoothness of the parameterized surface curve and the best fit of this curve to the 3D image data. We apply the complete method to real and synthetic problems, showing all steps in the process including the segmentation of image stacks, the polygonal surface mapping to the sphere, the fitting to SH series expansions and the calculation of final surface properties. In order to evaluate the quality of the SHP, we calculate the values of volume, surface area and mean-square curvature for synthetic data and compare them with the actual values as well as the values obtained using other segmentation methods.

2. Theory

2.1. Spherical harmonics parameterization

The SHs are the 3D equivalent of the Fourier series, and form a complete basis that allows the description of general stellar surfaces as functions r of the spherical coordinates (θ, ϕ) in a series expansion,

$$r(\theta,\phi) = \sum_{L=0}^{\infty} \sum_{K=-L}^{L} C_{LK} y_{LK}(\theta,\phi) \tag{1}$$

where $0 < \theta < \pi$ and $0 < \phi < 2\pi$. The C_{LK}s are the expansion coefficients, indexed by the integers L and K with $-L \leqslant K \leqslant L$ and $0 \leqslant L \leqslant \infty$. $y_{LK}(\theta,\phi)$ are the real symmetric and anti-symmetric combinations of the spherical harmonic basis functions given by

$$y_{LK}(\theta,\phi) = N_{LK} P_{L,K}(\cos\theta)\cos(K\phi) \quad \text{when } K \geqslant 0, \tag{2}$$

and

$$y_{LK}(\theta,\phi) = N_{LK} P_{L,K}(\cos\theta)\sin(|K|\phi) \quad \text{when } K < 0, \tag{3}$$

where $P_{L,K}(\cos\theta)$ are the associated Legendre polynomials (expressions for calculating them recursively are given in Appendix A.1) and N_{LK} are normalization constants (Hobson, 1955).

In order to describe surfaces regardless of whether they are stellar or not, we use the SH description in its parametric form (Duncan and Olson, 1993; Brechbühler et al., 1995). A surface $\vec{S}$ that is topologically equivalent to the sphere (i.e. of genus zero), can be represented as

$$\vec{S}(\theta,\phi) = \begin{bmatrix} x \\ y \\ z \end{bmatrix} = \begin{bmatrix} X(\theta,\phi) \\ Y(\theta,\phi) \\ Z(\theta,\phi) \end{bmatrix} \tag{4}$$

where $X(\theta,\phi)$, $Y(\theta,\phi)$ and $Z(\theta,\phi)$ are coordinate functions of θ and ϕ.

$$\begin{aligned} X(\theta,\phi) &= \sum_{L=0}^{\infty}\sum_{K=-L}^{L} C_{LK}^{X} y_{LK}(\theta,\phi) \\ Y(\theta,\phi) &= \sum_{L=0}^{\infty}\sum_{K=-L}^{L} C_{LK}^{Y} y_{LK}(\theta,\phi) \\ Z(\theta,\phi) &= \sum_{L=0}^{\infty}\sum_{K=-L}^{L} C_{LK}^{Z} y_{LK}(\theta,\phi) \end{aligned} \tag{5}$$

The three sets of expansion coefficients $(C_{LK}^{X}, C_{LK}^{Y}, C_{LK}^{Z})$ completely define the shape. There are three points we would like to note here. (a) This spherical harmonics parameterization is a highly economical way of generating stellar and non-stellar shapes. (b) The nature of this parameterization allows the creation of high curvatures (cusps) even when using low order harmonics, which can potentially be problematic in the absence of constraints on the smoothness of the surface. Both these properties can be explored with an in-house developed program called the SHAPE explorer (Spherical HArmonics Parameterization Explorer) which gives the user the ability to vary C_{LK} *s* and observe the resulting shapes in an interactive manner. The program can be downloaded at http://www.mpi-cbg.de/~khairy/ links.html. And (c), during the numerical implementation of SH calculations, the basis set has to be truncated at some maximum L value ($L_{\max}$).

Eq. (5) represents spherical harmonic synthesis, in which the given C_{LK}s can be used to construct the surface. In spherical harmonic analysis, the C_{LK}s are calculated from the individual Cartesian coordinate data whose values are defined on the unit sphere. The C_{LK}s are calculated according to

$$C_{LK}^{X} = \int_{0}^{2\pi}\int_{0}^{\pi} X(\theta,\phi) y_{LK}(\theta,\phi)\sin\theta\,\mathrm{d}\theta\,\mathrm{d}\phi \tag{6}$$

with similar equations for $Y(\theta,\phi)$ and $Z(\theta,\phi)$.

2.2. Parametric deconvolution

Parametric deconvolution involves refining a starting set of shape coefficients through direct fitting in image space in order to find the surface that gives a best fit to the experimental data. Assuming zero background and an amplitude α for the foreground intensity I_r, (i.e. the surface model) this could be done by minimizing

$$\chi^2(\vec{S},\alpha) = \sum_{i=1}^{N}\left(I_{\mathrm{d},i} - \alpha(I_{\mathrm{r},i}(\vec{S}) \otimes \Phi)\right)^2 \tag{7}$$

where the summation is performed over all voxels $i = 1,\ldots,N$, with $I_{\mathrm{d},i}$ the intensity of the ith voxel of the raw data, $I_{\mathrm{r},i}$ the intensity of the ith voxel of the reconstructed binary volume based on the surface $\vec{S}$ (see Section 3.3). Φ is the PSF of the microscope (in our case a theoretical estimate of it), and the symbol $\otimes$ denotes convolution. However, because image data is in general corrupted by noise, the minimization of Eq. (7) is an ill-posed problem and we must add a regularization (smoothing) term, which renders it well-posed. Regularization is also essential since the SHP tends to introduce artificial sharp edges, even at low L, as mentioned above. As a smoothing function we use the bending energy (E_{b}) of the surface. So our regularized problem is to minimize a functional $G(I_{\mathrm{d}},\vec{S})$ given by

$$G(\vec{S},\alpha) = \chi^2(\vec{S},\alpha) + \lambda E_{\mathrm{b}}(\vec{S}) \tag{8}$$

with λ the regularization parameter and E_{b} the normalized bending energy of the shape given by

$$E_{\mathrm{b}} = \left(\oint_{\vec{S}} (2H)^2\,\mathrm{d}A\right)/16\pi \tag{9}$$

where H is the local mean curvature of the contour, and the integration is performed over the area (A) of the closed shape. E_{b} is comparable to the internal energy commonly calculated for 2D and 3D snakes (Kass et al., 1988) and is proportional to the mean-squared mean curvature. λ determines the balance between the amount of smoothing (minimization of E_{b}) on the one hand and the closeness of the fit to the data on the other.

A central problem in inverse problem theory is the determination of the regularization parameter λ. The most popular methods for automatically determining regularization parameters are: minimizing the generalized cross-validation function (Wahba, 1990), minimizing a Bayesian information criterion (Akaike, 1980), and the L-curve method (Hansen, 1997). Generalized cross-validation is too computationally expensive for our problem, and the Bayesian information criterion penalizes the complexity of our shape description rather than accounting for our prior physical knowledge about the smoothness of the shape. Instead, we have chosen the L-curve method because it is computationally practical, and can be used to incorporate smoothness criteria. It depends on finding the point of maximum curvature on the usually L-shaped curve obtained when plotting the logarithm of the residual function (first term in Eq. (8)) *vs.* the logarithm of the smoothing function (in our case the bending energy; second term in Eq. (8)) for a series of values of the regularization parameter λ, i.e. every point on the L-curve is obtained from an optimization of Eq. (8) for a given λ. The optimal λ is determined graphically as the one corresponding to the corner of the resulting L-curve (see arrows in Figs. 4c and 5b). After minimizing Eq. (8) with the proper λ, confidence limits on the obtained parameters and shape properties can be determined from the covariance matrix of the estimates at the solution.

3. Computational methods

In this section we give an outline of our approach (Fig. 1). In short, the first two steps focus on the important problem of obtaining a good starting set of C_{LK}s. The 3D fluorescence image in the form of a stack of sections

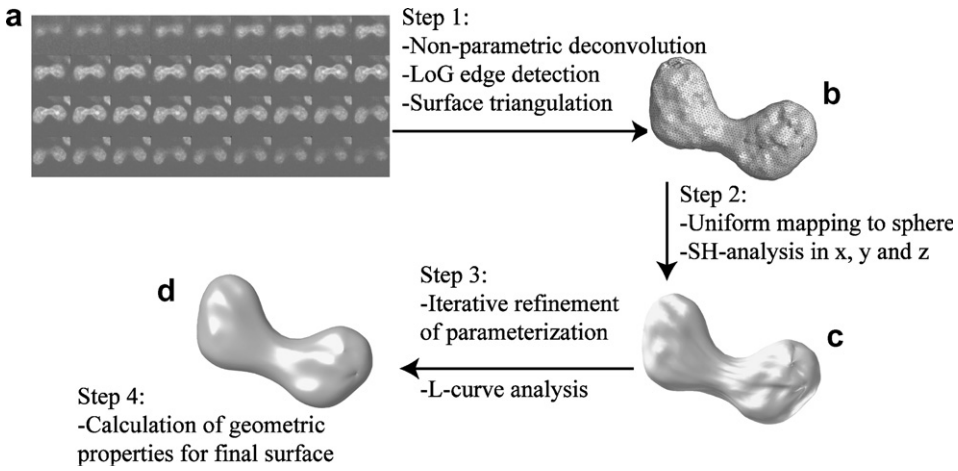

Fig. 1. General scheme for 3D parametric deconvolution. (a) Confocal microscopy sections of a fluorescently membrane-labelled live yeast zygote in meiosis 1. The raw data are shown. (b) Triangulated surface resulting from step 1. (c) Spherical harmonics parameterization of (b). (d) Parametrically deconvolved surface: the cell membrane contour corresponds to refined shape parameters which were fitted to the raw data (step 3).

(Fig. 1a) is non-parametrically deconvolved using commercial software and a theoretically determined (or experimentally measured) PSF and then intensity-thresholded. From the resulting point-cloud a surface triangulation is generated (Fig. 1b). This is followed by the critical step of uniformly mapping the triangulated surface to a parametric sphere. The three Cartesian coordinates of the shape, corresponding to the mapped vertices, are then expanded in spherical harmonic functions (Eq. (6)), providing a starting parametric approximation to the surface (Fig. 1c). To be able to calculate a measure of match between this shape and the image data (in our case χ^2), a complete intensity volume is constructed and to mimic the original data– convolved with the theoretical PSF of the microscope.

Parameter set refinement proceeds by iteratively fitting the intensity volume corresponding to the surface, to the raw data by varying the shape coefficients and the amplitude (α) of the foreground intensity (Eq. (8)). Changes to the coefficients introduced during the fitting are assumed to be small enough so as not to necessitate a modification of the initial spherical mapping. The fitting is repeated for a range of λ values and an L-curve is constructed. Our final surface (Fig. 1d) is the one fitted with the λ value that corresponds to the corner of the L-curve, which we determine graphically. From that final set of fitted coefficients the geometrical properties such as area (A), enclosed volume (V) and curvatures can be calculated (Appendix A.2). In the remainder of this section we highlight some details involved in carrying out the above steps.

3.1. Initial segmentation

Even though the fluorescent dye is highly specific in the ideal case, one often observes nonspecific labeling of other cellular structures (see Figs. 1a and 5a and Section 4.2.). This necessitates a segmentation step prior to surface finding. The non-parametrically deconvolved data is thresholded using Laplacian-of-Gaussian (LoG) edge detection (Marr and Hildreth, 1980) and an isosurface is produced using the marching cubes algorithm (Lorensen and Cline, 1987). In cases where the signal-to-noise is very low, Gaussian or median filtering prior to the thresholding may be necessary. Still, depending on the exact implementation and the quality of the data, the surface may contain holes and the triangle faces produced may be thin, elongated and with largely varying surface areas. In such cases, we fit a surface to the point-cloud data with radial basis functions (RBFs), using available fast routines (Carr et al., 2001). The polygonalization of the RBF is performed using a marching tetrahedra variant that has been optimized for surface following (Treece et al., 1999). The resulting mesh is of high quality; triangles are approximately of equal area and not highly sheared. The radial basis functions can be reliably used for surface interpolation (hole filling) as well (Carr et al., 1997). It should be stressed that any other scheme that results in a proper surface triangulation can be used here.

3.2. Surface mapping

After obtaining the surface triangulation, each surface point (x, y, z) is mapped onto a point (θ, ϕ) on the surface of the unit sphere (parameter space). This has to be accomplished while maintaining connectivity and nearest neighbors, preserving relative triangle area (triangles in the original surface mesh should have the same relative area as the corresponding geodesic triangles in parameter space) and if necessary minimizing triangle (shear) deformation.

The first step in the topological mapping is the unique mapping of surface points to the unit sphere. Here, we follow the method of (Brechbühler et al., 1995) modified for triangulated surfaces. Two poles are chosen in the surface mesh for the latitude (θ) calculation. One is identified as the "North pole" (θ_N) and the second as the "South pole" (θ_S). The exact choice of which points in the mesh to take is not critical, however it will influence the path taken by the

uniform mapping optimization later. For a scheme to choose the poles see (Shen and Makedon, 2004). A Laplace equation $\nabla^2\theta = 0$, with Dirichlet conditions $\theta_N = 0$ and $\theta_S = \pi$ is solved for θ. This is equivalent to solving the stationary heat diffusion equation over the surface mesh while cooling the North Pole and heating the South Pole. To calculate the longitude ϕ, a date line is introduced along which ϕ is incremented or decremented by 2π. The cyclic Laplace equation $\nabla^2\phi = 0$ is then solved. Each vertex has then associated with it a unique (θ, ϕ) coordinate, and can be placed on the unit sphere. The Laplace equations are solved by constructing a sparse linear system of dimensions equal to the number of vertices of the triangulation (Brechbühler et al., 1995), and then solving the linear problem using the biconjugate gradients algorithm with preconditioners calculated from an incomplete LU factorization (Press et al., 1992).

For a proper final shape representation the vertices must be uniformly distributed on the unit sphere (Brechbühler et al., 1995; Shen and Makedon, 2006). Throughout this work we relied on a fine high quality triangulation of the shape, for which only area preservation needed to be considered. The problem is to minimize

$$\sum_i^m \left(\frac{a_{p,i}}{4\pi} - \frac{a_{o,i}}{\sum_i a_{o,i}} \right)^2 \tag{10}$$

where $a_{p,i}$ is the geodesic area of triangle $i = 1,2,\ldots,m$, on the parametric sphere, $a_{o,i}$ is the area of triangle i on the original object. Let $\boldsymbol{A}$ be the vector of constraints on triangle areas of length m $\left(\boldsymbol{A}_i = a_{p,i}/4\pi - a_{o,i}/\sum_i^m a_{o,i}\right)$, and $\boldsymbol{C}$ represent the current configuration, a vector of length $2 \times n$ of θ and ϕ coordinates, where n is the number of vertices, then the problem is to find $d\boldsymbol{C}$ that renders,

$$\boldsymbol{A}(\boldsymbol{C} + d\boldsymbol{C}) = 0 \tag{11}$$

To first order, we can write,

$$\boldsymbol{A}(\boldsymbol{C} + d\boldsymbol{C}) = \boldsymbol{A}(\boldsymbol{C}) + \boldsymbol{J}^T(\boldsymbol{C}) \cdot d\boldsymbol{C} \tag{12}$$

where $\boldsymbol{J}$ is the $2n \times m$ Jacobian matrix of the areas given by

$$\boldsymbol{J} = \begin{bmatrix} \frac{\partial A_1}{\partial C_1} & \cdots & \frac{\partial A_m}{\partial C_1} \\ \vdots & \ddots & \vdots \\ \frac{\partial A_1}{\partial C_{2n}} & \cdots & \frac{\partial A_m}{\partial C_{2n}} \end{bmatrix} \tag{13}$$

Using Eqs. (11) and (12), we take Newton steps by iteratively solving for $d\boldsymbol{C}$,

$$-\boldsymbol{A}(\boldsymbol{C}) = \boldsymbol{J}^T(\boldsymbol{C}) \cdot d\boldsymbol{C} \tag{14}$$

and incrementing C with dC. Since, we have more variables than constraints ($2n > m$), Eq. (14) has many solutions. We choose the shortest possible $d\boldsymbol{C}$, which restricts $d\boldsymbol{C}$ to the column space of $\boldsymbol{J}$. So $d\boldsymbol{C}$ can be given by $d\boldsymbol{C} = \boldsymbol{J}(\boldsymbol{C}) \cdot d\boldsymbol{S}$, and the final linear system that is iteratively solved is,

$$\boldsymbol{J}^T\boldsymbol{J}d\boldsymbol{S} = -\boldsymbol{A}(\boldsymbol{C}) \tag{15}$$

where we increment $\boldsymbol{C}$ with $\delta\boldsymbol{J}d\boldsymbol{S}$ at each iteration, δ being a step length that can be determined by a line search. Eq. (15) forms a large sparse system that we solve using the GMRES algorithm (Saad and Schulz, 1986). In our implementation, we made the procedure significantly more CPU efficient by determining the sparsity pattern of $\boldsymbol{J}$ beforehand. Iterations proceed until a predetermined tolerance on $\boldsymbol{A}$ is met. After the uniform mapping the coordinates are expanded individually in a SH series (Eq. (6)). We choose the basis set truncation by increasing L_{max} until E_b of the shape increases, marking the onset of ringing. Criteria for choosing L_{max} based on Bayesian statistics also exist (Sivia and Carlile, 1992).

We show the application of our method on the spherical parameterization of a surface triangulation of the statue of Max-Planck's head (Fig. 2). More surface detail is revealed with increasing L_{max}, as would be expected from a converging Fourier series. We also tested the convergence of our method for shapes of known C_{LK}s with increasing mesh size (Fig. 3). These designed surfaces represent human red blood cell shapes and are of a level of complexity commonly encountered in biology.

3.3. Constructing the intensity volume from a set of shape parameters

The complete image volume (I_r of Eq. (7)) is simulated by: (1) initializing an image volume of twice the matrix dimensions as the raw data with all voxels set to zero, (2) calculating a shape triangulation, based on the starting parameters, on a fine mesh (triangles should not span across more than one voxel when overlaying the surface with the image volume), (3) assigning the value 1 to voxels that are intersected by surface triangles, which is possible since the synthetic volume forms a coordinate system that can directly be used by the surface, (4) integrating the intensity volume to obtain the final image size and finally (5) convolving the (binary) volume by the PSF corresponding to the optical system to obtain the simulated intensity volume. Since, we exclusively work with image dimensions that are powers of 2, we use the fast Fourier transform for the latter step. At each optimization step, I_r is multiplied by the best fitting foreground intensity amplitude (α in Eq. (7)).

3.4. Model optimization

For the minimization of the expression in Eq. (8), we use an unconstrained quasi-Newton nonlinear optimization algorithm, with the Broyden–Fletcher–Goldfarb–Shanno (BFGS) scheme for updating the Hessian matrix approximation (Broyden, 1970). However, BFGS fails to find a minimum (a) when the starting shape is far from the "true" one, in which case the optimization must be performed within a CPU-expensive hierarchical framework where

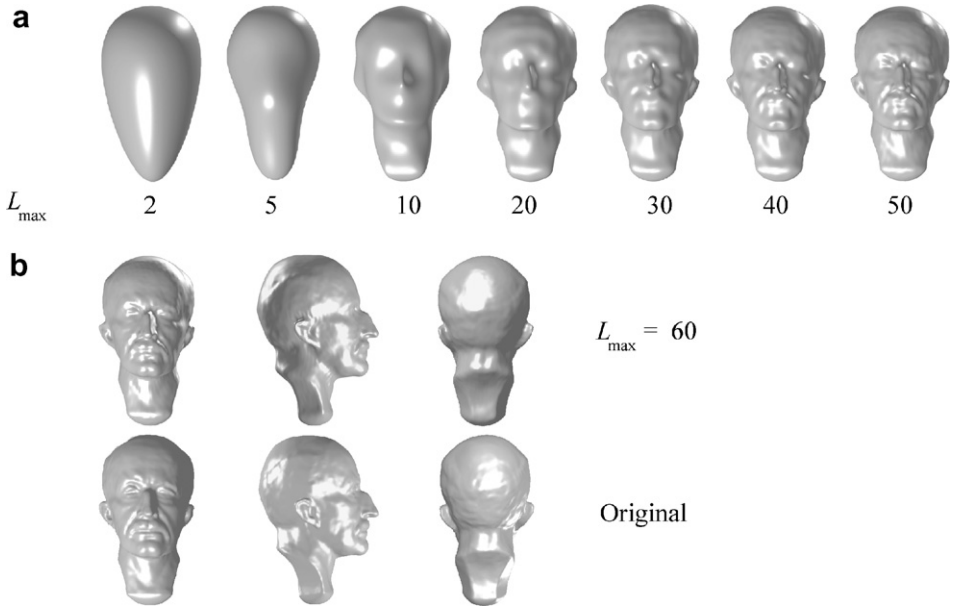

Fig. 2. Parameterization of the Max-Planck head obtained by preserving relative triangle areas in the spherical mapping step. (a) Increasing surface detail by gradually increasing L_{max} (Eq. (6)). (b) SHP surfaces at $L_{max} = 60$ and original. At $L_{max} = 60$ there are $(L_{max} + 1)^2 = 3721$ coefficients/coordinate for a total of 11,163 coefficients most of which are negligible. Only 234 of them have a value larger than 0.1% of the largest coefficient.

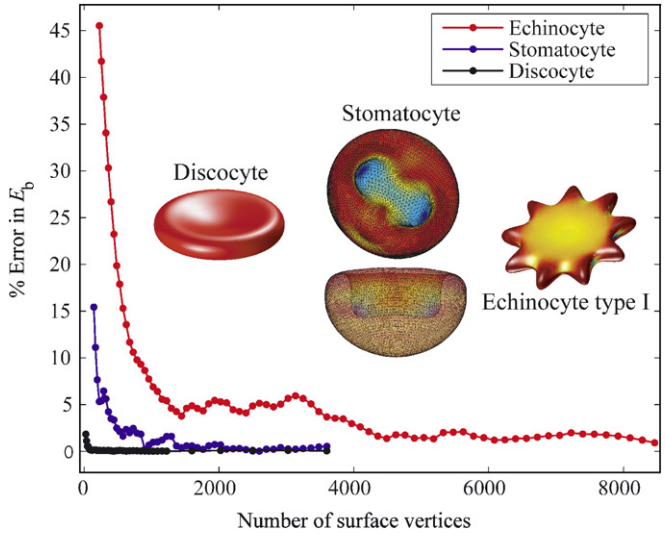

Fig. 3. Convergence of the surface mapping with increasing mesh size for three synthetic triangular surfaces that represent typical human RBC shapes. As a measure of convergence the bending energy was used.

both the raw and simulated data sets are convolved with 3D Gaussians of gradually decreasing width, and (b) when the value of λ is small to the extent that the problem is not regularized anymore. The amplitude α is adjusted by linear least squares at every step.

3.5. Shape correspondence between two SH-parameterized shapes

A unitless measure of correspondence between two SH-parameterized shapes a and b can be given by

$$R_{a,b} = 1 - \frac{\sum_{i=1}^{3\times(L_{max}+1)^2} (C^{a,i} - C^{b,i})^2}{\sum_{i=1}^{3\times(L_{max}+1)^2} ((C^{a,i})^2 + (C^{b,i})^2)} \quad (16)$$

where $3 \times (L_{max} + 1)^2$ corresponds to the total number of coefficients that describe a shape, and the $C^{a,i}$s and $C^{b,i}$s represent the ith corresponding shape coefficients that have been transformed into their translational and rotational invariant form (Brechbühler et al., 1995). $R_{a,b}$ approaches unity as two shapes approach each other. Thus it is a measure of the similarity of two shapes. For the reader to get a feeling for the values of R, we list some here for the shapes shown in Fig. 3: $R_{\text{Stomatocyte,Stomatocyte}} = 1.0$, $R_{\text{Discocyte,Stomatocyte}} = 0.890$, $R_{\text{Stomatocyte,Echinocyte}} = 0.871$. Note that the correspondence measure based on Eq. (16) requires that the spherical mapping be the same for the two shapes. However, we reasoned that if two different spherical mappings are both of high quality, then the correspondence measure based on Eq. (16) would still be meaningful and we sometimes also made this calculation (two values in Table 1 are from different mappings and this is indicated in the legend). In our experience the bending energy of Eq. (9) also serves as a sensitive measure of shape correspondence.

4. Results and discussion

The proposed scheme for parametric deconvolution is applied on both synthetic and real fluorescence microscopy data sets. All equations in this paper have been coded and executed within the Matlab programming environment and all surfaces were visualized using the Matlab "patch" function. All numerical calculations for shape properties were performed on surface meshes subjected to the stringent test

Table 1
Geometrical properties for surfaces shown in Figs. 1 and 4

		A (μm^2)[a]	V (μm^3)[a]	E_b[a]	$R_{a,b}$[a]
Yeast cell (Fig. 1)	Starting[b] (Fig. 1c)	170.1	132.8		
	Final (Fig. 1d)	165.2 ± 4.9	128.5 ± 3.8		$R_{\text{Final,Start}} = 0.970$
	Starting[c]	157.2	136.3		
	Final[c]	161.3 ± 5.1	128.0 ± 3.9		$R_{\text{Final,Final}}$[c] $= 0.995$
Stomatocyte (Fig. 4)	Triangulation	148.2	99.0	2.72	$R_{\text{Start,True}} = 0.970$[d]
	Starting[b]	141.6	100.1	2.59	
	Final	140.1 ± 1.3	100.2 ± 1.0	2.58 ± 0.08	$R_{\text{Final,Start}} = 0.998$
	True	139.6	99.7	2.57	$R_{\text{Final,True}} = 0.999$[d]

[a] Area (A), volume (V), normalized bending energy (E_b) and shape-correspondence measure ($R_{a,b}$) were calculated using Eqs. (A.9), (A.10), (9) and (16), respectively. Errors are standard errors of the mean.
[b] 3D image was non-parametrically deconvolved, segmented using Laplacian-of-Gaussian filter (LoG), mapped to the sphere and SH-parameterized (with $L_{\max} = 10$ for fission yeast, $L_{\max} = 22$ for stomatocyte).
[c] No non-parametric deconvolution. The raw image was segmented using LoG, mapped to the sphere and SH-parameterized (with $L_{\max} = 10$).
[d] The shapes compared are SH-parameterized based on two different spherical mappings.

that the integral of the Gaussian curvature deviated from its expected value of 4π (for the spherical topology equation (A.14)) by less than 0.1%.

4.1. Recovery of a synthetic shape from 3D pseudo image data

To test our parametric deconvolution scheme we first used it to recover a shape whose properties we know beforehand (Fig. 4). We designed a shape corresponding to a human red blood cell stomatocyte (Fig. 4a inset, also a local mean curvature color-coded version of this surface can be seen in Fig. 3 center) of known C_{LK}s ($L_{\max} = 22$), and simulated a corresponding $128 \times 128 \times 128$ voxel intensity volume (voxel dimensions $0.10 \times 0.10 \times 0.15\ \mu m^3$) as described in Section 3.3, except that Poisson (photon shot) noise was included prior to convolution with the theoretical PSF. A Poisson distribution of mean equal to the original intensity, with a base background intensity of 10% of the foreground was used to replace the image voxel intensities. This intensity volume served as a simulation of confocal microscopy image stacks (our "raw data", I_d of Eq. (7), Fig. 4a). The dataset was then analyzed, as described in Section 3. The starting shape was obtained by optimizing the mapping using area preservation only and expanding the shape at $L_{\max} = 22$. An L-curve with λ values ranging from 10^{-5} to 10^4 was constructed (Fig. 4c). The best value of λ was determined at the L-curve corner graphically (Fig. 4c, arrow) and found to be equal to $10^{3.15}$ in this example. The optimal shape is not separately shown, because it is almost indistinguishable from the original (see text and Table 1). Note that at too high values of λ, the optimization is shifted in favor of minimizing the bending energy, the fitted shape looses sharp features (Fig. 4b, inset) and its corresponding intensity volume visibly departs from the raw data (Fig. 4b) (the corresponding surface is shown in the inset; top and perspective views). The SH-coefficients corresponding to the best λ were used to calculate the shape properties (A, V, E_b) and then were compared to the properties of the original shape (Table 1). There was good agreement considering the uncertainties in the shape properties estimated from the C_{LK}s uncertainties (determined from the covariance matrix).

4.2. Parametric deconvolution of a real data set

An example of the application of parametric deconvolution to a real cell is shown in Fig. 5. A fission yeast

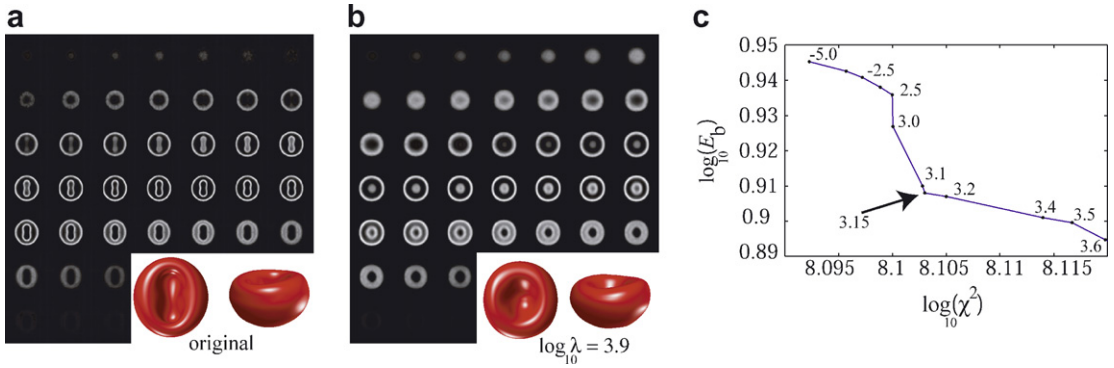

Fig. 4. Recovery of a simulated stomatocyte surface. (a) Simulated "raw data" stacks based on shape shown in the inset, (b) intensity volume of best fit (minimum of Eq. (8)) for a non-optimal choice of regularization parameter ($\lambda = 3.9$), (c) part of an L-curve generated by minimizing Eq. (8) for a range of λ values (from 1×10^{-5} to 1×10^4). Numbers next to the data points represent $\log_{10}(\lambda)$. The optimal λ is determined as the corner of the L-curve (arrow).

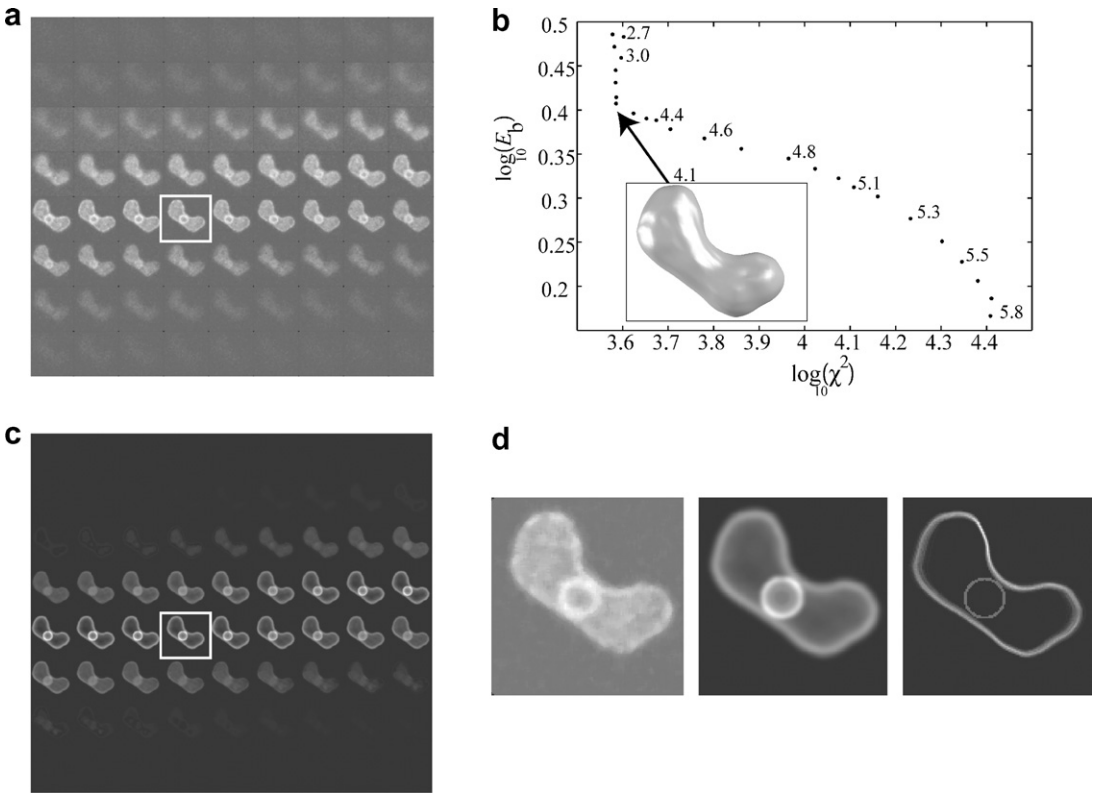

Fig. 5. Application of parametric deconvolution to a fission yeast cell. (a) Raw intensity data. (b) L-curve generated by minimizing Eq. (8) for a range of λ values (from $1 \times 10^{2.7}$ to $1 \times 10^{5.8}$), inset: cell surface corresponding to λ of $1 \times 10^{4.1}$. (c) Simulated intensity volume for the cell shape at optimal regularization parameter value ($\lambda = 4.1$). (d) Left and middle: enlarged 128×128 image frames corresponding to the white boxes in (a) and (c) respectively, right: "probability image" constructed from the deconvolved surface ((b) inset).

(*Schizosaccharomyces pombe*) zygote in meiosis I was membrane-labeled with a fluorescent dye so both cell membrane and round nuclear envelope can clearly be seen in the confocal stacks (Fig. 5a). Note that the image is complicated by uptake of dye into internal membranes, which gives the impression of there being both membrane and cytoplasmic labeling. Furthermore, the dye is incorporated into the nuclear envelope membrane, so that the spherical nucleus is also seen. The nucleus was included in constructing I_r of Eq. (7) as a sphere (Fig. 5c and d), which added four parameters to the optimization; three for the *xyz* coordinates of the center and one for radius. The L-curve was generated for λ values ranging from $10^{2.7}$ to $10^{5.8}$ (Fig. 5b). Note that the slight oscillations at the upper left hand corner in Fig. 5b are explained by the low regularization parameter value, so the problem is not well-posed in this regime. Although the output of the parametric deconvolution is a surface (a set of C_{LK}s with their corresponding variances), to stress the "image sharpening" effect of our deconvolution procedure, we have used the shape corresponding to the optimal set of C_{LK}s (Fig. 5b inset) to construct a "probability image" that reflects the uncertainties in the C_{LK}s (Fig. 5d, right). It is constructed by adding 50 images, corresponding to random draws from a Gaussian distribution with the optimal C_{LK}s as mean and width corresponding to individual C_{LK} standard deviations. (The variances were obtained from the covariance matrix calculated at the end of the optimization when $\lambda = 10^{4.1}$). This probability image shows which "regions" of the surface are well determined by the data (sharp lines) as opposed to the more diffuse parts of the contour.

4.3. Comparison with non-parametric deconvolution + segmentation and method consistency

One may ask how the above results compare with standard segmentation methods to find a surface in a 3D image. Our non-parametric deconvolution followed by edge detection, which we used to generate a starting shape, is such a standard segmentation method. We compare the geometrical properties of the starting and final shapes of Figs. 1 and 4 in Table 1. In case of the stomatocyte of Fig. 4, the shape-correspondence measure (Eq. (16)) between the starting parameterized shape and the true shape was 0.970, as opposed to $R_{\mathrm{Final,True}} = 0.999$, which shows that the parametric deconvolution process led to improvement.

To test the independence of our method on the starting shape we reanalyzed the fission yeast cell of Fig. 1 leaving out the initial non-parametric deconvolution. We segmented the image using LoG, triangulated and mapped the surface to the sphere and then parameterized the sur-

face, thus deliberately generating a worse starting shape, which was then used for our parametric deconvolution and the construction of the L-curve. Reaching a minimum (for every λ value) took significantly longer (due to the larger departure of the starting guess from the true shape), but the shape correspondence between the resulting surface and that when the analysis used non-parametric deconvolution gave a reassuring shape correspondence value of 0.995.

And finally a note on the computational requirements: the first significant bottle-neck is the uniform mapping on the parametric sphere surface (Fig. 1 Step 2), which for the surface of Fig. 4a (inset) required 9s for 100 GMRES iterations (+15 s for Jacobian pattern calculation) on a 2.5 GHz dual processor Macintosh with 4 GB RAM and a mesh size of 3600 vertices. Our termination criterion of minimum relative decrease in the function to be minimized of 1% was met within <100 iterations. When both triangle area and triangle shear were optimized simultaneously, 26 unconstrained Newton optimization iterations (3 min) were needed for convergence.

The most time-limiting computation is the minimization of Eq. (8); between ~1 h to ~20 h depending critically on the quality of the starting shape, the size of the intensity volume and the noise level. We need to perform this optimization many times (>20) during the construction of a satisfactory L-curve.

Though in both these examples the refined shapes are quite close to the initial triangulated surfaces, our procedure has two advantages that justify its use. The first is that the area and bending energy calculated from the parameterization are significantly better estimated than those from the surface triangulation, which always lead to overestimations. And the second is that parametric deconvolution provides uncertainties on all the geometric properties.

5. Summary

In this work, we have introduced a method for the parametric deconvolution of 3D microscopy images that enables the quantitative estimation of geometric properties when the object under study is topologically equivalent to the sphere. This applies to organelles, cells and many other biological and non-biological objects. Keys to our method are (a) use of the spherical harmonic parameterization representation of the object surface which enables us to perform (b) parametric 3D deconvolution, and (c) use of the L-curve graph for finding the proper balance between fitting the data and incorporating our prior knowledge about the contour. We advocate the use of the SHP and with this work believe to have increased its accessibility to a broad base of users.

Acknowledgements

We thank Dr. Iva Tolic-Norrelykke and Ms. Isabel Raabe for the *Schizosaccharomyces pombe* images. We thank Dr. JiJinn Foo for discussions about practical issues of biological imaging. Many thanks also go to Dr. Martin Styner and Dr. Yannis Kalaidzidis for numerous helpful discussions on the spherical parameterization and regularization in signal processing. This work was funded by the Max Planck Society.

Appendix A

A.1. Calculation of $P_{L,K}$s and their derivatives

The $P_{L,K}$s are calculated using backward recursion relations (Hobson, 1955). For each integer $L \geqslant 0$ the value of $P_{L,L}(\cos\theta)$ is evaluated using the relation

$$P_{L,L}(\cos(\theta)) = \frac{(2L)!}{L!}\left(\frac{1}{2}\sin\theta\right)^{L} \tag{A.1}$$

The remaining values $P_{L,K-1}(\cos\theta)$ are calculated from $P_{L,K}(\cos\theta)$ and $P_{L,K+1}(\cos\theta)$ as follows:

$$\begin{aligned}&(L+K)(L-K+1)P_{L,K-1}(\cos\theta)\\&\quad = 2K\cot(\theta)P_{L,K}(\cos\theta) - P_{L,K+1}(\cos\theta)\end{aligned} \tag{A.2}$$

where $P_{L,K}(\cos\theta) = 0$ when $K > L$. These relations have been analysed for accuracy and numerical stability (Wiggins and Saito, 1971).

The first and second derivatives of the associated Legendre polynomials with respect to $\theta(P'_{L,K} = \mathrm{d}P_{L,K}/\mathrm{d}\theta$ and $P''_{L,K} = \mathrm{d}^2P_{L,K}/\mathrm{d}\theta^2)$, respectively, are needed for the calculation of the surface vectors to obtain the geometric quantities (Eqs. (A.9), (A.10), (A.11), (A.12), (A.13), (A.14)). The following relations were used in this work:

$$P'_{L,L}(\cos\theta) = \frac{L(2L)!}{2L!}\left(\frac{1}{2}\sin\theta\right)^{L-1}\cos\theta \tag{A.3}$$

$$P''_{L,L}(\cos\theta) = -\frac{L(2L)!}{4L!}\left(\frac{1}{2}\sin\theta\right)^{L-2}(1 - L\cos^2\theta) \tag{A.4}$$

The derivatives of the remaining terms are given by the recursion relations,

$$\begin{aligned}&(L+K)(L-K+1)P'_{L,K-1}(\cos\theta)\\&\quad = 2K\cot\theta P'_{L,K}(\cos\theta) - 2K\csc^2\theta P_{L,K}(\cos\theta) - P'_{L,K+1}(\cos\theta)\end{aligned} \tag{A.5}$$

and

$$\begin{aligned}&(L+K)(L-K+1)P''_{L,K-1}(\cos\theta)\\&\quad = 2K\cot\theta P''_{L,K}(\cos\theta) - 2\csc^2\theta P'_{L,K}(\cos\theta) + 2\\&\qquad \times \cot\theta\csc^2\theta P_{L,K}(\cos\theta)\end{aligned} \tag{A.6}$$

A.2. Calculation of shape properties from SH-coefficients

The spherical harmonics coefficients encode all surface properties of the shape. The formulae for calculating these properties are obtained from results of classical differential geometry (O'Neill, 1997). The normal vector to the surface is given by

$$\vec{n} = \frac{\vec{S}_\theta \times \vec{S}_\phi}{|\vec{S}_\theta \times \vec{S}_\phi|} \tag{A.7}$$

where $\vec{S}_\theta$ and $\vec{S}_\phi$ are 3-vectors,

$$\vec{S}_\theta = \begin{bmatrix} \sum_{L=0}^{\infty} \sum_{K=-L}^{L} C_{LK}^{X} \frac{\partial Y_{LK}(\theta,\phi)}{\partial \theta} \\ \sum_{L=0}^{\infty} \sum_{K=-L}^{L} C_{LK}^{Y} \frac{\partial Y_{LK}(\theta,\phi)}{\partial \theta} \\ \sum_{L=0}^{\infty} \sum_{K=-L}^{L} C_{LK}^{Z} \frac{\partial Y_{LK}(\theta,\phi)}{\partial \theta} \end{bmatrix} \tag{A.8}$$

similarly for $\vec{S}_\phi$, and the second derivatives.

The total surface area A and volume V are given by,

$$A = \int_0^{2\pi} \int_0^{\pi} |\vec{S}_\theta \times \vec{S}_\phi| \mathrm{d}\theta \mathrm{d}\phi \tag{A.9}$$

$$V = \frac{1}{3} \int_0^{2\pi} \int_0^{\pi} (\vec{S} \cdot \vec{n}) |\vec{S}_\theta \times \vec{S}_\phi| \mathrm{d}\theta \mathrm{d}\phi \tag{A.10}$$

The coefficients of the first (E, F, G) and second (L, M, N) fundamental forms are given in terms of the surface differentials, normals, and derivatives of the normal vector by,

$$\begin{aligned} E &= \vec{S}_\theta \cdot \vec{S}_\theta \\ F &= \vec{S}_\theta \cdot \vec{S}_\phi \\ G &= \vec{S}_\phi \cdot \vec{S}_\phi \\ L &= -\vec{S}_\theta \cdot \vec{n}_\theta \\ M &= \frac{1}{2}(\vec{S}_\theta \cdot \vec{n}_\phi + \vec{S}_\phi \cdot \vec{n}_\theta) \\ N &= -\vec{S}_\phi \cdot \vec{n}_\phi \end{aligned} \tag{A.11}$$

With the above coefficients we can calculate the local mean curvature H as

$$H = \frac{EN + GL - 2FM}{2(EG - F^2)} \tag{A.12}$$

which is needed for calculating E_b (Eq. (9)).

As a self-check for the accuracy of our procedure and its implementation we also calculate the Gaussian curvature (K)

$$K = \frac{LN - M^2}{EG - F^2} \tag{A.13}$$

which when integrated over a closed surface of spherical topology must satisfy,

$$k = \frac{1}{4\pi} \int_{\vec{S}} K \, \mathrm{d}A = 1 \tag{A.14}$$

Eqs. (9), (A.9), (A.10) and (A.14) are integrated numerically using Gaussian quadrature (Scarborough, 1966).

References

Akaike, H., 1980. Likelihood and the Bayes procedure. In: Basian Statistics. University Press, Valencia, Spain, pp. 143–166.

Brechbühler, C., Gerig, G., Kuebler, O., 1995. Parametrization of closed surfaces for 3-D shape description. Computer Vision and Image Understanding 61 (2), 154–170.

Broyden, C., 1970. The convergence of a class of double-rank minimization algorithms II: The new. J. Inst. Math. Appl. 6, 222–231.

Carr, J.C., Fright, W.R., Beatson, R.K., 1997. Surface interpolation with radial basis functions for medical imaging. IEEE Transactions on Medical Imaging 16 (1), 96–107.

Carr, J.C., Beatson, R.K., Cherrie, J.B., Mitchell, T.J., Fright, W.R., McCallum, B.C., Evans, T.R., 2001. Reconstruction and representation of 3D objects with radial basis functions. In: SIGGRAPH 2001, Computer Graphics Proceedings, ACM Press / ACM SIGGRAPH. Los Angeles, CA, pp. 67–76.

Duncan, B.S., Olson, A.J., 1993. Approximation and characterization of molecular surfaces. Biopolymers 33 (2), 219–229.

Gerig, G., Styner, M., Jones, D., Weinberger, D.R., Lieberman, J.A., 2001. Shape analysis of brain ventricles using SPHARM. In: IEEE Workshop on Mathematical Methods in Biomedical Image Analysis, pp. 171-178.

Hansen, P.C., 1997. Rank-deficient and discrete ill-posed problems: numerical aspects of linear inversion. SIAM, Philadelphia.

Hobson, E.W., 1955. The Theory of Spherical and Ellipsoidal Harmonics. Chelsea, New York.

Jansson, P., 1996. Deconvolution of Images and Spectra. Academic Press Inc., Orlando, FL, USA.

Kass, M., Witkin, A., Terzopoulos, D., 1988. Snakes: active contour models. International Journal of Computer Vision 1, 321–331.

Kelemen, A., Székely, G., Gerig, G., 1999. Elastic model-based segmentation of 3-D neuroradiological data sets. IEEE Transactions on Medical Imaging 18 (10), 828–839.

Lipowsky, R., 1991. The conformation of membranes. Nature 349, 475–481.

Lorensen, W.E., Cline, H.E., 1987. A high resolution 3D surface construction algorithm. Computer Graphics 21 (4), 163–169.

Marr, D., Hildreth, E.C., 1980. Theory of edge detection. Proceedings of the Royal Society of London, Series B. 207, 187–217.

McMahon, H.T., Gallop, J.L., 2005. Membrane curvature and mechanisms of dynamic cell membrane remodelling. Nature 438 (7068), 590–596.

O'Neill, B., 1997. Elementary Differential Geometery. Academic Press, San Diego.

Press, W.H., Teukolsky, S.A., Vetterling, W.T., Flannery, B.P., 1992. Numerical Recipes in C. Cambridge University Press.

Saad, Y., Schulz, M., 1986. SIAM Journal on Scientific and Statistical Computing 7, 856–869.

Scarborough, J.B., 1966. Numerical Mathematical Analysis. John Hopkins Press, Baltimore.

Sezekely, G., Kelemen, A., Brechbuehler, C., Gerig, G., 1996. Segmentation of 2-D and 3-D objects from MRI volume data using constrained elastic deformations of flexible Fourier contour and surface models. Medical Image Analysis 1 (1), 19–34.

Shen, L., Makedon, F., 2004. Spherical parameterization for 3D surface analysis in volumetric images. In: The International Conference on Information Technology: Coding and Computing (ITCC'04), pp. 643–649.

Shen, L., Makedon, F., 2006. Spherical mapping for processing of 3D closed surfaces. Image and Vision Computing 24, 743–761.

Sivia, D.S., Carlile, C.J., 1992. Molecular spectroscopy and Bayesian spectral analysis – How many lines are there? Journal of Chemical Physics 96 (1), 170–178.

Staib, L.H., Duncan, J.S., 1996. Model-based deformable surface finding for medical images. IEEE Transactions on Medical Imaging 15 (5), 720–731.

Styner, M., Lieberman, J.A., McClure, R.K., Weinberger, D.R., Jones, D.W., Gerig, G., 2005. Morphometric analysis of lateral ventricles in schizophrenia and healthy controls regarding genetic and disease-specific factors. PNAS 102 (13), 4872–4877.

Terzopoulos, D., Witkin, A., Kass, M., 1988. Constraints on deformable models: recovering 3D shape and nonrigid motion. Artificial Intelligence 36 (1), 91–123.

Treece, G.M., Prager, R.W., Gee, A.H., 1999. Regularized marching tetrahedra: improved iso-surface extraction. Computers and Graphics 23 (4), 583–598.

Verveer, P., Gemkow, M., Jovin, T., 1999. A comparison of image restoration approaches applied to three-dimensional confocal and wide-field fluorescence microscopy. Journal of Microscopy 193 (1), 50–61.

Wahba, G., 1990. Spline Models for Observational Data. SIAM, Philadelphia.

Wiggins, R.A., Saito, M., 1971. Evaluation of computational algorithms for the associated legendre polynomials by interval analysis. Bulletin of the Seismological Society of America 61 (2), 375–381.